2018

Sentinel-2 as a tool for quantifying suspended particulate matter in the Tamar Estuary, UK

Wright, D.

Wright, D. (2018) 'Sentinel-2 as a tool for quantifying suspended particulate matter in the Tamar Estuary, UK', The Plymouth Student Scientist, 11(2), p. 3-33.
http://hdl.handle.net/10026.1/14182

The Plymouth Student Scientist
University of Plymouth

*The Plymouth Student Scientist, 2018, **11**, (2), 3-33*

Sentinel-2 as a tool for quantifying suspended particulate matter in the Tamar Estuary, UK

Duncan Wright

Project Advisor: Dr Jill Schwarz, School Biological and Marine Sciences,
Plymouth University, Drake Circus, Plymouth, PL4 8AA

Abstract

This project explores the potential use of Sentinel-2 as a tool for quantifying suspended particulate matter (SPM) in the Tamar estuary. In the first section of this project, the radiometric performance of Sentinel-2B is quantified using *in situ* above-surface reflectance data acquired autonomously off the waters of Lanai, Hawaii. Three band ratio algorithms were tested/developed for atmospheric correction over this location. No band ratio performed best, but greater inaccuracies were found using the red/green bands (RD -27 – -87 % at 560nm, RD 312 – 440 % at 665nm) in contrast to the blue bands (443nm (RD 4 – 11 %) and 491nm bands (RD -8 – -17 %). This was attributed to inadequate signal to noise ratios over clear waters. In the second section *in situ* SPM data alongside radiometric data were used to derive four SPM algorithms. The best performing algorithm was found to be a green/blue ratio, which utilised the 560nm and 497nm bands of Sentinel-2A ($R^2 = 0.761$, p-value < 0.01, N = 15). The empirically derived exponential algorithm was subsequently applied to two Sentinel-2A tiles (25th January 2017 and 26th March 2017) to map SPM throughout the estuary. A river plume extending into the Sound in Figure 11 (LW + 0.5) and slightly higher in Figure 12 (LW + 1.5) were observed. There was no evidence of an estuarine turbidity maximum in either image. When comparing derived SPM results with values from the literature it is clear that the algorithm underestimated SPM in both images. The primary reason for the underestimation of SPM in the estuary was thought to be due to a failure in atmospheric correction.

Introduction

ESA's new high resolution land observation satellite pair known as Sentinel-2 offers an exciting new opportunity for the observation of small scale coastal processes. However this is only possible if the signal-to-noise (SNR) statistics are adequate and accurate atmospheric correction is attainable (Pahlevan, et al., 2017). SNR performance can be problematic as if it is too low it is difficult to differentiate the reflected signal from sensor noise. In this first section of this project, atmospheric correction will be performed utilising the ACOLITE processor. Using three different band combinations, TOA Sentinel-2 data was atmospherically corrected and the results will be tested against in situ data collected autonomously off the waters of Lanai, Hawaii.

SPM is a primary measure of water quality (European Union, 2008) and is of interest to the bio-optical community (Nechad, et al., 2010). Obtaining SPM data from high resolution remote sensing satellites offers a cheap and regular data source. Given the optical complexity of estuarine waters and sensor specific variations it is necessary to develop regional and sensor specific algorithms. In the second section of this project an empirical suspended particulate matter (SPM) algorithm will be developed for the Tamar estuary.

Background Review

Coastal Monitoring

There are various forms of SPM found within the water column. These can range from colloids 1 nm – 1 μm in size to organisms of the order of millimetres (Jackson, et al., 1997). In coastal waters, the concentration of inorganic particles is considerably higher than that of open waters. This is due to the runoff of clays, sands and silts (Bowers & Binding, 2006). In this project SPM is defined as particulate matter larger than 0.7 μm in diameter.

The quantification of SPM in coastal waters is a key measure of water quality (European Union, 2008), as well being of interest to the bio-optical community (Nechad, et al., 2010). SPM concentrations influence a variety of biogeochemical processes. Increased SPM directly limits photosynthetic growth (Platt, et al., 1988), as increased concentrations of suspended sediment prevent light from passing through the water column (Kirk, 2011). SPM is also relevant to sediment transport, sediment resuspension (Acker, et al., 2002) and the transfer of heat into the upper waters (Morel & Antoine, 1994). Finer particles also enhance microbial growth as smaller particles offer the highest surface area to volume ratio for them to settle on (Hoppe, 1984).

Optical Properties of Sediments

The scattering and absorption properties of suspended sediments affect the attenuation of light through the water column. The spectral influence of these sediments varies with the composition and distribution of sediment particle size (Maul, 2012), as well as particle shape and mineraology (Novo, et al., 1989).

Particulate absorption varies widely from place to place (different coloured water bodies indicate different absorption characteristics). However, when comparing the absorption spectra of mineral suspended solids (MSS) in the literature some consistent patterns emerge. MSS absorption spectra have been analysed from the Irish Sea (Harker, 1997) (Bowers & Binding, 2006), Saharan dust samples (Babin &

Stramski, 2002) and from Italian river samples (Tassin & Ferrari, 2003). All absorption spectra generally decreased with increasing wavelength, and all spectra exhibited a small shoulder at around 500 nm.

In general, sediment absorption and scattering charcteristics are non-linear and vary with various properties such as particle size, colour, density and shape all influencing the scattering and absorption of light through the water column (Mobley, 1994).

Using the methodology and instrumentation developed by Kirk (1994), Bowers et al. (1998) were able to directly measure the reflection and diffuse attenuation coefficients at various stations in the Irish Sea to derive absorption and scattering coefficients. They observed that 64% of the variation in mineral specific scattering of light was related to particle density (mass concentration/volume concentration) and only 15% of the total variance was related to particle diameter.

Sediment Dynamics in Estuaries

Three modes of sediment transport occur in coastal waters: Wash load, bed load and suspension. Wash load comprises the smallest particles, generally consisting of fine clay material. These particles are kept in motion by turbulence and as they are so fine, move at all current speeds. Suspension occurs as a result of erosion of grains from the bed, and the transfer of kinetic energy to the grains because of turbulence. Particles smaller in diameter than 150 μm will go into suspension with any movement; particles larger than this move at higher velocities. Bed load describes the movement of coarser sediments moving along the bed and move via the process of saltation. As current velocities increase so too does the concentration of SPM and the mean grain size of that material (Dyer, 1995).

Flocculation describes the process in which suspended material clump together to form particulate matter. Flocculation rates are enhanced by increases in concentration of suspended material, grain inertia, shear velocity (McCave, 1975). Studies have also shown that exopolymer particles exuded by living organisms give rise to flocculation (Passow, et al., 1994; Alldredge & Silver, 1988).

In the estuarine environment sediments are a highly dynamic constituent, responding to a variety of oceanographic and meteorological processes. Tidal fluctuations influence resuspension, advection and disposition. Wind gives rise to stochastic resuspension events, and lower wind speeds negatively influence resuspension rates. Seasonal variations also impact suspended sediment rates. During the summer, thermal stratification stimulates the growth of phytoplankton species which gives rise to changes in organic sediment. This leads to increased flocculation rates and therefore larger particles; this increases settling rates and reduces the total suspended sediment load (Jones, et al., 1998).

The estuarine turbidity maximum (ETM) is one of the most notable features of sediment dynamics in the estuarine environment, occurring in meso- (<2m tidal range) and macrotidal (4-6m tidal range) estuaries. The ETM (sometimes referred to as the estuarine turbidity zone, ETZ) is the zone in which the quantity of suspended sediment is highest. The strong tidal influence in these meso/macrotidal estuaries is capable of holding a high concentration of sediment in suspension whilst also preventing particles from settling. A high proportion of the fine sediment in the estuary is held within this zone, and the residence time of these fine sediments can be in excess of one year (Dyer, 1995). In macrotidal estuaries the tidal range difference between springs and neaps is considerable; this leads to large variations in the position and magnitude of the ETM (Allen, et al., 1980). In addition to this, seasonal changes in river flow rate also influence the position and strength of the ETM. Reduced river flow leads to a weaker ETM that is higher up the estuary and higher river flow leads to a stronger ETM that is closer to the estuary mouth (Dyer, 1995).

Study Site 1: The MOBY Buoy, Hawaii

The Marine Optical Buoy (MOBY) is located 20km off the Hawaiian island of Lanai (Figure 1), where the depth is approximately 1200m.

Figure 1: MOBY buoy, Hawaii (Google Maps, 2018).

At this station, since July 1997, MOBY has measured downwelling irradiance and upwelling radiance for the calibration of many ocean colour sensors. MOBY currently measures downwelling irradiance onto the sea surface as well as upwelling radiance at 1, 5 and 9 and metres below the sea surface. The final reprocessed water-leaving radiance dataset has a typical uncertainty of less than 5%, however variations in the environment may add further uncertainty (Clark, et al., 2000).

The MOBY buoy is in consistently case 1 waters with minimal biological activity (Clark, et al., 2000). Case 1 waters are defined as waters with high chlorophyll concentrations in comparison to particulate matter concentrations (Morel & Prieur, 1977). The Hawaiin islands are located in the centre of the North Pacific subtropical gyre. Due to the gyres anticyclonic circulation pattern, the upper water column is almost completely isolated from neighbouring current systems (Karl & Lukas, 1996). As a result of this, temperature, salinity and dissolved inorganic nutreints are relatively constant laterally (Hayward, 1991). Seasonal variations in the upper waters and surface mixed layer are also uncommon (Bingham & Lukas, 1996). The gyre has a generally permanent nutricline and pyncoline, which is even present during the winter months. As a result, the upper waters are continuously oligotrophic and produce organic matter at a low rate. The main source of nutrients is thought to be from periodic injections such as biological migrations, nitrogen fixation, atmospheric inputs and episodic deep sea mixing (Karl & Lukas, 1996).

Study Site 2: The Tamar Estuary

The Tamar estuary (Figure 2) is located in the South West of England, dividing South Devon and North Cornwall.

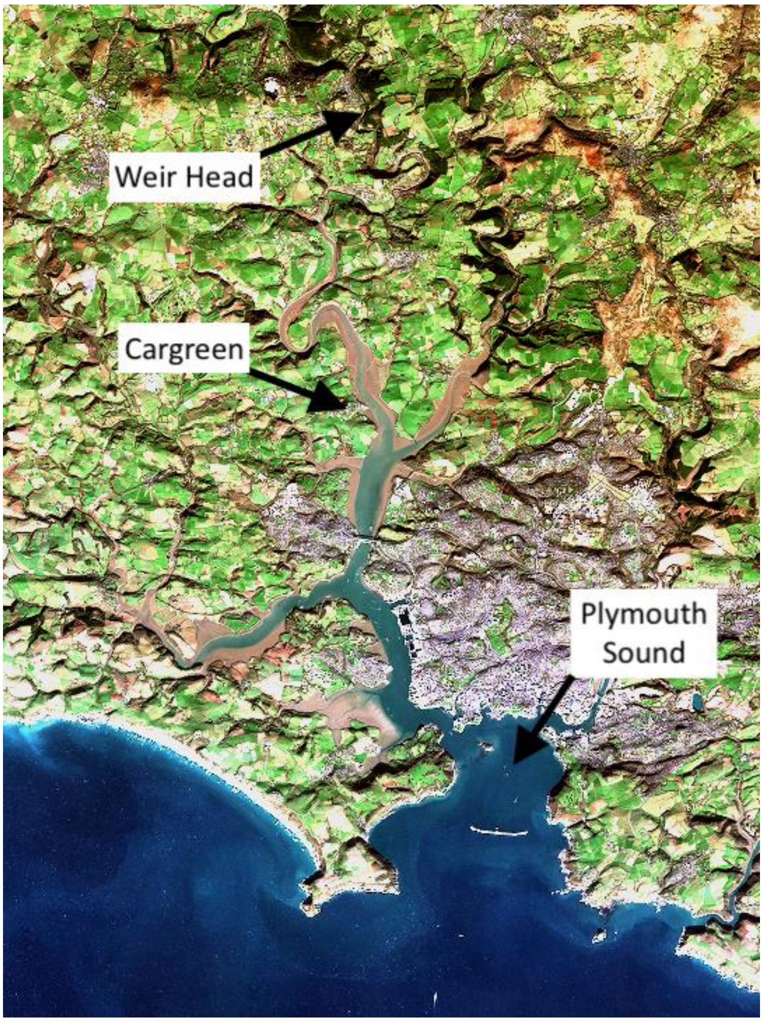

Figure 2: The Tamar estuary as seen from Sentinel-2A (25th January 2017). Credit: ESA/Sentinel-2A/MSI – *CC BY-SA IGO 3.0* license.

The estuary is tidal for 31km, spanning from Plymouth Sound to Weir Head. In the top 20km of the estuary (Weir Head – Cargreen) the mean depth is 2 – 8m below mean high water springs. In the final 11km the channel deepens significantly with depths ranging from 8 to 40m below mean high water springs (Grabemann, et al., 1997). The estuary is semi-diurnal and hypersynchronous, i.e. the effect of convergence exceeds the frictional effect and thus the tidal range is larger toward the estuary head and lower in the upper riverine section (Dyer, 1995).

Uncles & Stephens (1989) found that the ETM in the Tamar holds the highest quantity of suspended sediment when it is in the lower reaches of the estuary. They also observed a net landward sediment flux during summer due to the asymmetric tide, where the flood phase current velocities are stronger than during the ebb phase and thus more sediment can be carried in suspension. In winter, when the river flow is higher, the sediment transported up the estuary in the summer is redeposited downstream and thus the sediment flux is balanced. Because of the seasonal fluctuations in river flow, the position of the ETM during the summer is in the upper reaches of the estuary and moves down during the winter to the mid-estuary as a result of increased river flow (Uncles & Stephens, 1989) (Uncles & Stephens, 1993). The ETM during springs is clearly defined and reaches maximum concentrations of 2 – 3 kg m^{-3}; during neaps the ETM is more dispersed and only reaches peaks of roughly 0.2 kg m^{-3} (Uncles, et al., 1994). At slack water, when current velocities slow, sediments fall out of suspension. During neaps, slack water periods are longer and as a result more sediment settles (Dyer, 1995).

Sentinel-2

The Sentinel-2 mission comprises two satellites, each carrying a MultiSpectral Instrument (MSI). Each MSI records data in 13 spectral bands at varying spectral resolution. The spatial resolution of these bands (at ground level) varies between 10, 20 and 60m; the swath width is 290km. The two satellites (Sentinel-2A and Sentinel-2B) follow the same sun-synchronous orbit with one delayed behind the other to increase revisit times, the revisit time at the equator is 5 days (Drusch, et al., 2012).

The Sentinel-2 mission is intended to provide monitoring of land usage. However, if the signal-to-noise ratio (SNR) performance statistics are acceptable and accurate atmospheric correction of L1C data is possible, Sentinel-2 will provide an invaluable tool for the monitoring of coastal and inland waters. Pahlevan, et al. (2017) took more than 30 L1C (top-of-atmosphere (TOA)) images over spatially uniform and clear waters and calculated average SNRs. These values are displayed in Table 1 alongside the Sentinel-2 technical specification.

Table 1: Sentinel-2A/Sentinel-2B wavelengths, spectral and spatial resolutions, specification SNRs (Gatti & Galoppo, 2018) and observed SNRs (Pahlevan, et al., 2017). * indicates the band width is the same for each satellite.

Band#	Central wavelength (S2A/S2B) (nm)	Band width (S2A/S2B) (nm)	Spatial Resolution (m)	Reference Radiance [W/m²/sr/µm]	SNR Requirement (at Lref)	Clear Water SNR Performance (Sentinel-2A TOA) (at Lref)
1	443.9/443	27/45	60	129	129	439
2	496.6/492.1	98*	10	128	154	102
3	560/559	45/46	10	128	168	79
4	664.5/665	38/39	10	108	142	45
5	703.9/703.8	19/20	10	74.5	117	45
6	740.2/739.1	18*	20	68	89	34
7	782.5/779.7	28*	20	67	105	26
8	835.1/883	145/133	10	103	174	20
8a	864.8/864	33/32	20	52.5	72	16
9	945/943.2	26/27	60	9	114	NA
10	1375.5/1376.9	75/76	60	6	50	NA
11	1613.7/1610.4	143/141	20	4	100	2.8
12	2202.4/2185.7	242/238	20	1.5	100	2.2

Ocean colour satellites MERIS and MODIS have quicker revisit times (1-3 days) than the Sentinel-2 satellites, but in this case the large spatial resolution (250m per pixel) means that the data is only suitable for the mapping of oceanographic properties in larger estuaries (e.g. SPM (Doxaran, et al., 2009; Nechad, et al., 2003)). Sentinel-2 is the first high resolution (10, 20, 60m per pixel) satellite to cover the world's coastal zone with revisit times of up to 5 days. This offers an exciting new opportunity to measure oceanographic properties at high spatial resolution from space. In relation to the two study sites covered in this study, the high spatial resolution of Sentinel-2 will allow for radiometric quantification of the Tamar's higher reaches and the revisit time of 1 - 5 days will increase the chance for cloudless matchups over both sites.

Additionally, with the introduction of the high quality SWIR bands, the potential for accurate atmospheric correction is improved. This is as absorption in these bands is extremely strong and reflectance can therefore be assumed to be zero (in clear waters), thus the remaining signal can be assumed to be caused by aerosol scattering only (Vanhellemont & Ruddick, 2016). Compared with Landsat-8's Operational Land Imager (OLI) instrument, MSI has four more bands in the NIR region (Table 1 bands 5-8a) at higher spectral resolution (D'Odorico, et al., 2013). These additional NIR bands increase accuracy of retreival of bio-optical paramerers in optically complex coastal and inland waters (IOCCG, 2000). In particular they provide improved retrievals of bio-optical parameters such as SPM/turbidity and Chlorophyll-a in highly turbid (Liu, et al., 2017; Lee, et al., 2016; Nechad, et al., 2016; Gernez, et al., 2015) and hypertrophic waters (Toming, et al., 2016; Kutser, et al., 2016; Watanabe, et al., 2017). In many highly turbid waters, organic detritus and suspended minerals scatter light beyond 700 nm. Thus it is useful to have additional NIR bands as longer wavelengths may be needed to be used to acquire a dark pixel for effective astmopheric correction (IOCCG, 2000).

Atmospheric Correction

To derive bio-optical parameters from satellite imagery the remote sensing reflectance ($R_{rs}(\lambda)$) must first be calculated. This is problematic as a large proportion (up to 90%) of the signal received by the satellite sensor is influenced by aerosols and sunglint reflected by air molecules in the atmosphere (Franz, et al., 2015) (Gordon, et al., 1997). The process of removing the effects the atmosphere has on the reflectance data is known as atmospheric correction. The effect the atmosphere has on the signal received by the satellite is influenced by various factors. These factors include water vapour, oxygen, carbon dioxide and ozone content, all of which alter the signal through molecular or aerosol absorption and scattering (Gao, et al., 2009). The signal is also influenced by geometric factors such as the angle of the view of the sensor, the solar elevation angle and the slope and position of the target in relation to the solar azimuth (Lantzanakis, et al., 2017). Two main types of atmospheric correction exist, physical-based and image-based. Physical-based atmospheric correction methods rely on radiative transfer models. They require auxiliary data on atmospheric optical properties coincident to the time the satellite image was taken. This data is commonly collected at a ground station or derived from satellite data (Lantzanakis, et al., 2017).

Atmospheric parameters have varying effects on the reflectance magnitude of different light spectra. For example, Vermote, et al. (1997) found that a change in atmospheric water vapour content of 0.5-4.1 g cm^{-2} led to a change in 3.4 – 14%

change in reflectance in the near-infrared (NIR) region, but only a change of 0.5 – 3% in the visible light region for the bands of Landsat 5’s Thematic Mapper. Atmospheric scattering effects also decay exponentially from shorter (blue) to longer (red/NIR) wavelengths, i.e. the TOA signal at shorter wavelengths comprises of more atmospheric signal than at longer wavelengths (Bodhaine, et al., 1999). This is problematic in the context of bio-optical remote sensing as band ratios are commonly used to derive bio-optical parameters. For example, Chlorophyll-a and CDOM algorithms commonly use blue/green band ratios, therefore they are more prone to the skewed spectral influence of atmospheric scattering (Matthews, 2011).

Image-based atmospheric correction methods derive atmospheric effects from the image itself and then remove them from the TOA reflectance to get bottom-of-atmosphere (BOA) reflectance. ACOLITE is an example of an image-based atmospheric correction method (Vanhellemont & Ruddick, 2016). This correction method was developed specifically for marine applications. ACOLITE uses Look-Up Tables (LUTs) generated with a radiative transfer model (6SV) (Vermote, et al., 2006) to estimate Rayleigh scattering. Under the assumption of high pure water absorption in the NIR/SWIR wavelengths, the remaining signal after Rayleigh correction can be assumed to be caused by aerosol scattering alone (Gordon & Wang, 1994). The ratio of the two chosen bands (in the NIR or SWIR region) can then be used to extrapolate the aerosol reflectance into the visible wavelengths (Yang & Gordon, 1997). Note that the atmospheric correction can use any combination of two bands given the requirement that the water-leaving signal in these bands is known or negligible (Franz, et al., 2015).

SPM from Remote Sensing Data

Carrying out SPM measurements from a boat is time consuming and expensive. The deployment of automated sensors reduces costs, however data are limited spatially (i.e. at one point) and most estuaries do not have sensors present (Etcheber, et al., 2011).

The determination of SPM via remote sensing data is cheap (using public satellites) and measurements are regular. Satellite derived SPM data has many uses; Van Raaphorst, et al. (1998) used AVHRR SPM data in conjunction with *in situ* data to produce sediment transport maps. Lacroix, et al. (2007) used MERIS SPM data in a light forcing ecosystem model and Fettweis & Van den Eynde (2003) used SPM data as model input conditions as well as for model validation.

Landsat has been used to map and develop suspended sediment algorithms in various inland and coastal waters such as the Amazon River (Mertes, et al., 1993), the Gironde and Loire estuaries (Doxaran, et al., 2003; Doxaran, et al., 2006; Doxaran & Lavender, 2018), the Rhone River mouth (Forget & Ouillon, 1998), the Orinoco River (Yepez, et al., 2017). The latest Landsat satellite has a high spatial resolution (30m per pixel), which makes it suitable for observing small scale processes, however, due to its infrequent revisit time (16 days (Vanhellemont & Ruddick, 2016)), as an oceanographic tool, it is significantly temporally limited. Ocean colour satellites MERIS and MODIS have much quicker revisit times (1-3 days), but in this case the low spatial resolution (250m per pixel) means that this data is only suitable for the quantification of SPM in larger estuaries (Doxaran, et al., 2009) (Nechad, et al., 2003).

Given the non-linearity of SPM optics in the estuarine environment (Mobley, 1994) and the influence of other optically significant constituents such as coloured dissolved organic matter and phytoplankton pigments, it is necessary to develop a sensor specific, regional algorithms to accurately quantify SPM from Sentinel-2 data.

Forget & Ouillon (1998) developed an empirical algorithm for SPM based on *in situ* SPM and radiometric data collected at the mouth of the River Rhone. Log linear relationships ($R_{rs}(\lambda)$ vs log(TSM)) were derived using various bands of three satellite sensors (SPOT HRV 1/2 and Landsat ETM). Algorithms were developed for the following single bands: the 485 ± 35 nm, 560 ± 40 nm, 660 ± 30 nm bands of the ETM and the 545 ± 45 nm and 645 ± 35nm bands of SPOT HRV1/2. SPM concentrations varied between 1 and 80 mg L^{-1}. All bands exhibited a strong log linear relationship ($R^2 = 0.972 – 0.982$).

Doxaran, et al. (2003) developed empirical relationships for the quantification of SPM in the Grionde and Loire estuaries. They used band ratios to derive logarithmic relationships for each estuary using various sensors. In the Gironde Estuary they used the bands of SPOT (840 ± 50 nm/545 ± 45 nm, R^2 = 0.884) and Landsat (775 ± 25 nm/565 ± 40 nm, R^2 = 0.8816 and 775 ± 25 nm/482.5 ± 32.5 nm; R^2 = 0.8752); in the Loire Estuary they used the bands of SPOT (840 ± 50 nm/545 ± 45 nm R^2 = 0.9292) and SeaWiFS (865 ± 20 nm nm/555 ± 10 nm, R^2 = 0.9036). This data was later used to derive an algorithm for the bands of MODIS-Aqua and MODIS-Terra (Doxaran, et al., 2009). The authors then carried out a linear regression to compare the satellite derived SPM data with *in situ* SPM data acquired at the Marel platform in the Gironde estuary. R^2 values were as follows: Terra = 0.7653 and Aqua = 0.8235. Discrepencies between the results were attributed to seasonal variations that were not observed in the initial algorithm (Doxaran, et al., 2009).

Yepez, et al. (2017) developed an empirical algorithm using the NIR channel of Landsat-8 in the Orinoco River in Venezuela. Algorithms were also developed using the red channel (R^2 = 0.7308) and using a ratio between the two channels (NIR/red, R^2 = 0.8406), the NIR channel alone was chosen for the succeeding analysis as it gave the best fit (R^2 = 0.9928). They subsequently tested their algorithm with independently collected *in situ* data. It was found to fit with the following statistics, R^2 = 0.9127, bias = 7 %, root-mean-squared-error = 11.64 mg L^{-1}, relative-mean-error = -9.6% and standard deviation = 13.9 mg L^{-1}.

Doxaran & Lavender (n.d.) derived an empirical algorithm using a linear regression for the Tamar estuary. They used a band ratio derived for the bands of SPOT (840 ± 50 nm/545 ± 45 nm). They observed a strong relationship (R^2 = 0.9907) for SPM data between 10 – 350 mg L^{-1}, however this was only considered a premilinary results as only 6 *in situ* data points were used. Doxaran, et al. (2005) also developed an algorithm for the Tamar. They developed a linear relationship between total SPM and a 850 nm/550 nm band reflectance ratio.

Given the results of Doxaran & Lavender (n.d.) and Doxaran, et al. (2005) in the Tamar, the studies carried out in the Gironde and Loire estuaries (Doxaran, et al., 2003) and the work of Forget & Ouillon (1998) at the mouth of the Rhone River, two band ratios will be plotted as a function of total SPM: 865/560 and 665/560.

Methods

Sentinel-2 Data Acquisition: MOBY buoy

Sentinel-2 images were downloaded from the Copernicus Open Access Hub (https://scihub.copernicus.eu/). Data for comparison against MOBY buoy data were selected based on cloud coverage of the image (<1%) and if they coincided with the MOBY data acquisition times. Data that satisfied these criteria were available on the 27th of December 2017 and the 16th and 26th of January 2018 (3 images). The data were downloaded as Level-1C (L1C) products, which are 100x100 km^2. L1C products provide pixel-by-pixel TOA reflectance values on a Universal Transverse Mercator (UTM) projection (Gatti & Bertolini, 2017). Note that these images were acquired by the Sentinel-2B satellite.

ACOLITE Atmospheric Correction

Atmospheric correction was applied to the L1C images over the MOBY buoy using the ACOLITE processor. ACOLITE is available free of charge from the Royal Belgian Institute of Natural Sciences (http://odnature.naturalsciences.be/remsem/software-and-data/acolite/). The version used for this study was version 20170718.0. The remote sensing reflectance was calculated for all bands. Cloud masking was performed using the Rayleigh corrected reflectances in the SWIR band (B11 – 1610nm) with a cloud masking threshold of 2.15%. ACOLITE modifies Rayleigh reflectance data using a Second Simulation of the Satellite Signal in the Solar Spectrum (6SV) LUT; this takes into account sensor and sun geometry as well as sunglint, which is modelled for wind speed of 1 ms^{-1}. Under the assumption of high pure-water absorption in the NIR and SWIR bands, aerosol contribution was estimated using three band combinations: 665nm/885nm, 1612nm/2201nm and 885nm/2201nm on a per pixel basis (i.e. at native resolution). A standard atmospheric pressure of 1013.25 hPa was selected for Rayleigh processing (Vanhellemont & Ruddick, 2016). Reflectance values were then extracted from the output in SNAP (Sentinel Application Platform) at the location of the MOBY buoy (20.4903° N, -157.1141° E).

MOBY Buoy $R_{rs}(\lambda)$

MOBY has not been configured for the bands of Sentinel-2, so the bands of Sentinel-3 were used for the radiometric comparison; the bands used are shown below in Table 2. As all satellite overpass matchups were with Sentinel-2B, these bands are displayed below in Table 2.

Table 2: Bands used for radiometric comparison between in situ (Sentinel-3 bands; (Donlon, et al., 2012) and Sentinel-2B bands.

Sentinel-2B central wavelength (band #)	(MOBY) Sentinel-3 wavelength (band #)
442.3 (B1)	443 (Oa3)
492.1 (B2)	490 (Oa5)
559 (B3)	560 (Oa6)
665 (B4)	665 (Oa8)

$R_{rs}(\lambda)$ was calculated using the methods of Mobley (1999):

$$R_{rs}(sr^{-1}) = \frac{L_w}{E_d}$$

Equation 1: Remote Sensing Reflectance

where E_d (W m^{-2} nm^{-1}) is the downwelling irradiance at the surface and L_w (W m^{-2} sr^{-1} nm^{-1}) is the normalised water-leaving radiance.

Statistical Analysis

For analysis of the performance of each atmospheric correction the root-mean-squared-deviation (RMSD), bias and relative differences (RD) were calculated using the following equations:

$$RMSD(\lambda) = \frac{\sqrt{(\sum_{1}^{n=3} S2R_{rs}(\lambda) - MOBYR_{rs}(\lambda))}}{n}$$

Equation 2: Root-mean-squared-deviation

$$Bias(\lambda) = \frac{\sum_{1}^{n=3} S2R_{rs}(\lambda) - MOBYR_{rs}(\lambda)}{n}$$

Equation 3: Bias

$$RD(\lambda) = \frac{1}{n}\sum_{1}^{n=3}\frac{S2R_{rs}(\lambda) - MOBYR_{rs}(\lambda)}{MOBYR_{rs}(\lambda)} \times 100$$

Equation 4: Relative difference

Where $S2R_{rs}(\lambda)$ atmospherically corrected reflectance value from Sentinel-2 at a given wavelength and $MOBYR_{rs}(\lambda)$ is the MOBY derived *in situ* reflectance at a given wavelength.

Tamar Estuary: Above-Surface Remote Sensing Reflectance Data

All data obtained via these methods were acquired by the students of the MAR518 module. Cruises were conducted on the 27th, 28th, 30th and 31st of March 2017.

Spectral data was measured using a RAMSES-ARC spectroradiometer, recording radiance between 350 and 950 nm at approximately 3 nm resolution. Spectral data was recorded in pairs. The first reading was over a white plate (downwelling irradiant light) and the second over water (water-leaving radiance). $R_{rs}(\lambda)$ was then calculated using the methodology of Mobley (1999), as previously described. In post processing, for each station, the spectral pair with the lowest signal were selected for analysis, under the assumption these spectra were the least contaminated by reflection off the water's surface.

Sentinel-2 Data Acquisition: Tamar Estuary

Data were selected based on coincidence with the MAR518 module Tamar cruises. There were no exact temporal matchups, so a tile from the day before the cruise of the 27th was selected. For seasonal comparison a tile from the 25th of January was also selected. The data format for each tile was the same as for the MOBY tiles. However, note that the image acquired for the Tamar Estuary was taken using Sentinel-2A.

Tamar Estuary: SPM Data

All data obtained by these methods were acquired by the students of the MAR518 module. Cruises were conducted on the 27th, 28th, 30th and 31st of March 2017. The stations are displayed in Figure 3.

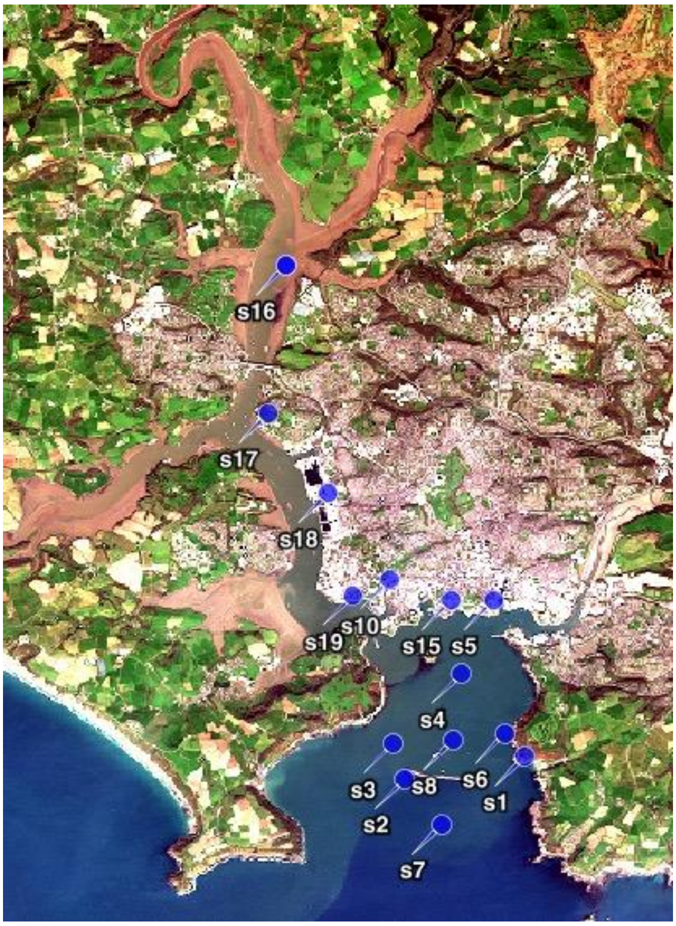

Figure 3: Survey stations map. Stations 1 – 5 (27th), stations 6 – 10 (28th), station 15 (30th) and stations 17 – 19 (31st). Credit: ESA/Sentinel-2A/MSI – *CC BY-SA IGO 3.0* license.

SPM concentrations were derived gravimetrically; this method was initially developed by Banse, et al. (1963), and was later adapted by Strickland & Parsons (1972) and Shimwell (1999).

Surface water samples were collected using a van Dorn water sampler. Water samples were then stored in pre-washed PTFE containers. Containers were rinsed three times with the sample to be stored before the final sample was taken. Whatman GF/F filters (nominal pore size of 0.7 μm) were first washed with purified water and then placed on aluminium foil. The foil sheets, along with filters, were placed in an oven at 60°C for one hour. They were then placed in a desiccator with a silicon desiccant for up to 3 days. Each filter was then weighed three times on a scale with 1x10^{-5} g precision.

A known volume of each water sample was filtered through the pre-weighed filters using a vacuum pump. Each filter was then placed in an aluminium foil sachet and stored at -20°C until analysis. Sachets were placed in an oven at 60°C overnight and then in a desiccator for up to 3 days. The filters were then weighed again. The initial filter weight was then subtracted from the final filter weight to give total SPM (organic plus inorganic).

Tamar Estuary: Tidal and Rainfall Data

Tidal data was acquired online from the British Oceanographic Data Centre (BODC) UK Tide Gauge Network. For the Tamar estuary, the BODC obtain tidal measurements from the Devonport tidal gauge (https://www.bodc.ac.uk/data/hosted_data_systems/sea_level/uk_tide_gauge_network/).

Daily rainfall data was acquired online, from a weather station in Crownhill, Plymouth (http://www.bearsbythesea.co.uk/wxrainsummary.php). The data selected for this study was from the 25th to the 27th of March 2017.

Modelling Sentinel-2A Bands and SPM Algorithm

In situ spectra acquired on the 27th, 28th, 30th and 31st of March 2017 at sixteen stations along the Tamar were recalculated for the bands of Sentinel-2A. This was achieved by averaging the *in situ* spectra over the central band ± the bandwidth of that band (i.e. averaged over 443.9 ± 13.5nm).

Four reflectance band ratios were plotted against SPM data. These comprised of two green/blue ratios (560nm/497nm and 560nm/443nm), a red/green ratio (655nm/560nm) and a NIR/green ratio (885nm/560nm). Subsequently, a log linear regression analysis was carried out in MATLAB, where SPM data was logarithmically transformed and the reflectance ratios remained linear. Confidence intervals were also applied (95 %). Suitability of fit for each algorithm was quantified via the R^2 value and the p-value (tested at $\alpha = 0.05$), these were also calculated in MATLAB.

An algorithm was then derived from the best performing reflectance ratio. After atmospheric correction, this algorithm was applied to two Sentinel-2A tiles (26th March 2017 and 25th January 2017). The atmospheric correction applied to this tile utilised the 865nm/2202nm band combination. The best performing reflectance ratio and the algorithm used are discussed in the Results and Discussion section.

Results and Discussion

MOBY Buoy: Assessment of Radiometric and Atmospheric Correction Performance

Figures 4 through 6 are Sentinel-2B images over the MOBY buoy. Sunglint is present in all images, as indicated visible striping (more pronounced in Figures 4 and 6). This is due to the near-nadir view of the MSI sensor, resulting in the radiance data being influenced by the reflection of sun at the air-water interface (Harmel, et al., 2018). This effect is more pronounced over the open ocean, where regular surface waves are present (Clerc, 2018).

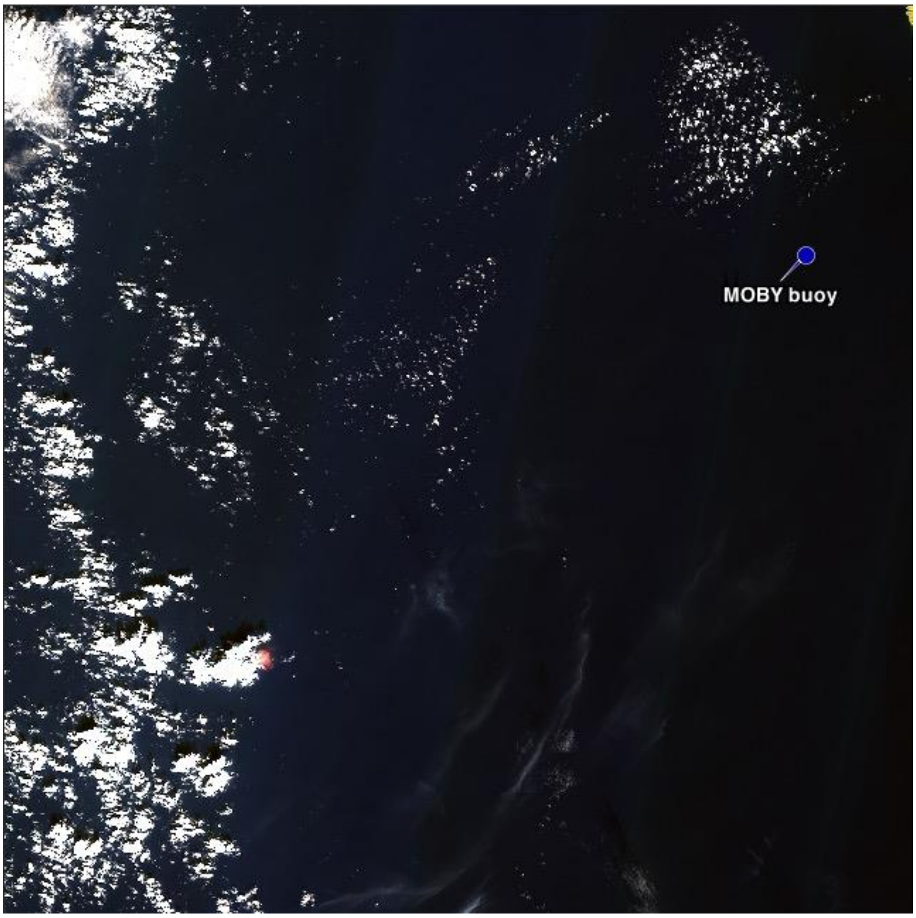

Figure 4: Sentinel-2 L1C image over the MOBY buoy, 26th December 2017. Credit: ESA/Sentinel-2B/MSI – *CC BY-SA IGO 3.0* license.

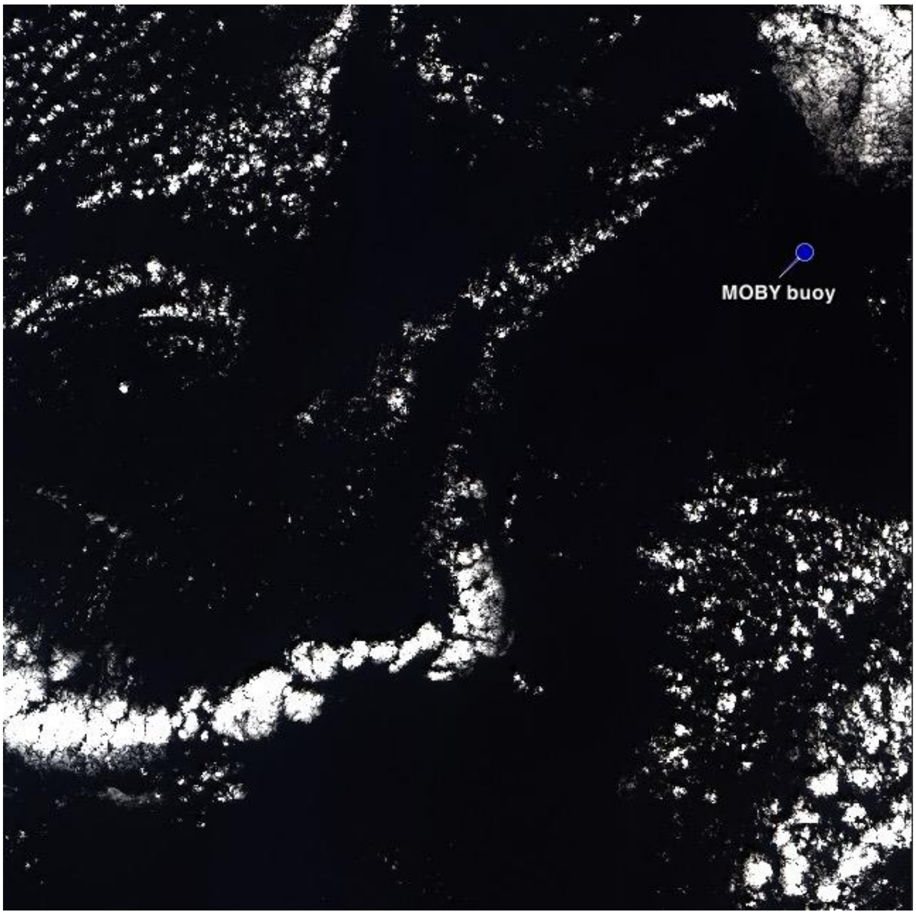

Figure 5: Sentinel-2 L1C image over the MOBY buoy, 11th January 2017. Credit: ESA/Sentinel-2B/MSI – *CC BY-SA IGO 3.0* license.

Table 3 shows the flyover times and geometric data for each image, alongside the MOBY data acquisition time. The images appear cloudless over the region of the buoy; however, it is not possible to know whether or not clouds were present over the buoy at the time of the flyover. All Sentinel-2B flyovers were near simultaneous (5-7 minutes) with the MOBY data acquisition (Table 3). It is therefore assumed that the optically significant constituents were the same between the flyover and the buoy data acquisition. Due to the short timeframe (within 1 month) in which the flyovers occurred, the solar angles are all relatively similar. This suggests the viewing geometry has minimal influence on differences in reflectance between images.

Table 3: MOBY data acquisition time and Sentinel-2 flyover time and geometric data

Matchup date	Sentinel-2 Flyover Time (UTC)	MOBY Data Acquisition Time (UTC)	Mean Solar Zenith Angle (°)	Mean Solar Azimuth Angle (°)	Mean Sensor Zenith Angle (°)	Mean Sensor Azimuth Angle (°)
2017/12/26	21:09:09	21:14:26	47.9	154.4	6.4	104.6
2018/01/16	21:09:19	21:16:04	46.7	150.4	6.4	104.5
2018/01/26	21:09:19	21:15:08	45	148.1	6.4	104.7

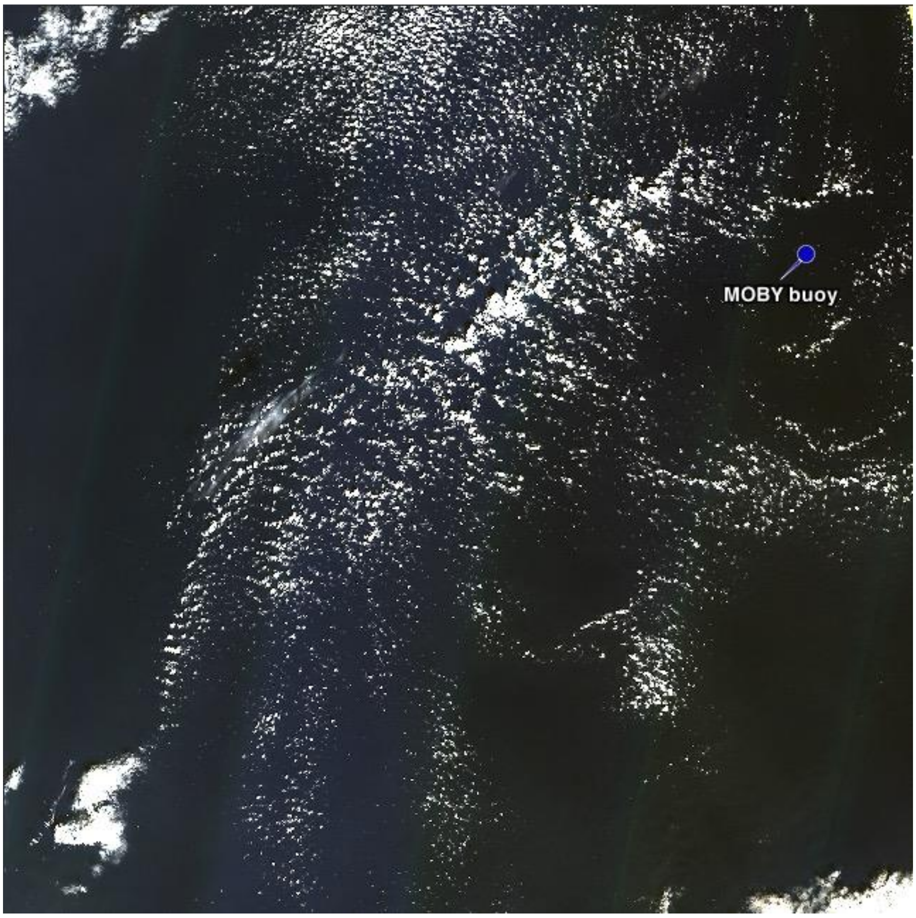

Figure 6: Sentinel-2 L1C image over the MOBY buoy, 26th January 2018. Credit: ESA/Sentinel-2B/MSI – *CC BY-SA IGO 3.0* license.

Based on the work of the Pahlevan, et al. (2017) the NIR/SWIR band combination were expected to perform best. This is as in the SWIR (2202nm) band absorption water is extremely high and in the NIR (865nm) band the SNR is higher than other wavelengths in the SWIR/NIR region, which allows for a more accurate quantification and removal of aerosol contribution (Franz, et al., 2015). However, no band combination worked consistently better than another across all four wavelengths.

In the 443nm band the red/NIR (665nm-865nm) and SWIR only (1613nm-2202nm) band combinations performed best (in red/NIR RMSD = 0.000000486 sr^{-1}, bias = -0.000323 sr^{-1}, RD = 4.2 % and in SWIR only RMSD = 0.000000429 sr^{-1}, bias = 0.000367 sr^{-1}, RD = 4.6 %), whereas in the 491nm and 560nm band the NIR/SWIR method (865nm-2202nm) performed best (@491nm RMSD = 0. 000000193 sr^{-1}, bias = -0.000517 sr^{-1}, RD = -8.2 % and @560nm RMSD = 0.0000000766 sr^{-1}, bias = -0.000353 sr^{-1}, RD = -27.0 %). In the 665nm band the SWIR only band combination performed best (RMSD = 0.0000000393 sr^{-1}, bias = -0.000277 sr^{-1}, RD = 311.6 %).

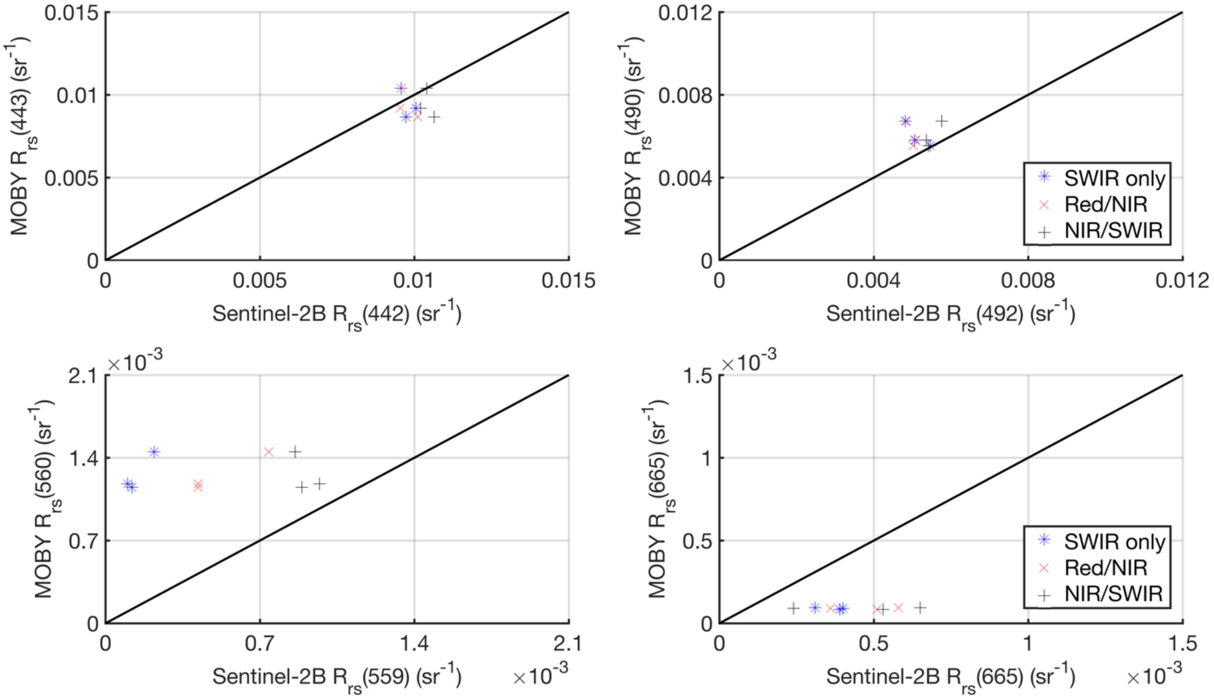

Figure 7: Scatter plot of in situ MOBY Rrs(λ) versus Sentinel-2B Rrs(λ) derived using the ACOLITE processor. Each window corresponds to the four (near) matching visible wavelengths, 443nm/442nm (top left), 490nm/492nm (top right), 560nm/559nm (bottom left) and 665nm/665nm (bottom right). The band combination for each method is as follows: SWIR only (1613nm-2202nm), Red/NIR (665nm-865nm) and NIR/SWIR (865nm-2202nm).

Table 4: Root-mean-squared-deviation (RMSD), bias and relative differences (RD) for in situ and atmospherically corrected Sentinel-2B data presented in Figure 7.

Band combination / wavelength (443nm)	RMSD (sr^{-1})	Bias (sr^{-1})	RD (%)
SWIR only (1613nm-2202nm)	0.000000429	0.000367	4.6
Red/NIR (665nm-865nm)	0.000000486	-0.000323	4.2
NIR/SWIR (865nm-2202nm)	0.000000823	0.000997	11.3
Band combination / wavelength (491nm)			
SWIR only (1613nm-2202nm)	0.000000703	-0.000913	-14.2
Red/NIR (665nm-865nm)	0.00000073	-0.00104	-16.6
NIR/SWIR (865nm-2202nm)	0.000000193	-0.000517	-8.2
Band combination / wavelength (560nm)			
SWIR only (1613nm-2202nm)	0.000000623	-0.00111	-88.6
Red/NIR (665nm-865nm)	0.000000269	0.000733	-59.0
NIR/SWIR (865nm-2202nm)	0.0000000766	-0.000353	-27.0
Band combination / wavelength (665nm)			
SWIR only (1613nm-2202nm)	0.0000000393	-0.000277	311.6
Red/NIR (665nm-865nm)	0.0000000817	0.000394	440.0
NIR/SWIR (865nm-2202nm)	0.0000000884	0.000384	428.1

It is challenging to draw any conclusions regarding which band combination performed best due to the low (n = 3) number of satellite and *in situ* data matchups and that each performed better at different wavelengths. It is however clear from the results that across all band combinations they performed worse at the red/green end of spectrum (RD -27 – -87 % at 560nm, RD 312 – 440 % at 665nm) in contrast to the 443nm (RD 4 – 11 %) and 491nm bands (RD -8 – -17 %).

Effective atmospheric correction depends on adequate SNRs as well as a sufficient digital resolution to store the water-leaving signal (Franz, et al., 2015). Given that the satellite values do not ‘bottom out’ (i.e. reach a detection limit), this would suggest the SNRs of MSI were not sufficient over this water type. Ocean satellites have the requirement of a SNR of 1000 in the 443nm band (Hu, et al., 2012). This potential inadequacy is supported by the results of Pahlevan, et al., 2017 (Table 1), which show the SNR of the MSI 443nm band at 439 over clear waters. The MSI SNRs decrease with increasing wavelength (439, 102, 79, 45 for the bands: 443nm, 491nm, 560nm, 665nm respectievely). This can be explained by the low productive waters the MOBY buoy is situated (Clark, et al., 2003). In these water types there is a minimal reflected signal in the green and red spectral region (hence low SNRs), which can most likely be attributed to the high absorption by pure water and the minimal particulate scattering at this end of the spectrum. At the blue end of the spectrum, the signal is greater as pure water absorption is not dominate (high SNRs) (Hu, et al., 2012). This explains the decreasing peformance of the atmospheric correction with increasing wavelength. In addition to this, inadequate SNRs in the bands used for atmospheric correction could lead to noise and bias across the visible spectrum. This is because of inaccuracies in calculating aerosol contribution to the signal, which is then used to extrapolate results to the visible spectra (Hu, et al., 2012). Insufficient SNRs in the atmospheric correction bands were also evident in the results of Pahlevan, et al., 2017 (Table 1) where SNRs at 665nm, 865nm, 1613nm and 2202nm equalled 45, 16, 2.8 and 2.2 respectively; these fall far below the requirements set by European Space Agency (2015) of SNRs of 142, 72, 100 and 100 (in the same order).

An additional source of error arises from the fact that ACOLITE does not correct for adjacency effects. Adjacency effects occur when a non-uniform reflecting surface is present. This causes radiance from the high reflective area to contaminate neighbouring weakly reflecting surfaces causing them to appear brighter than they actually are (Otterman & Fraser, 1979). In this case, the non-uniform reflecting surfaces are the clouds observed in Figures 4 - 6. Other potential sources of error include inaccurate aerosol models, shading of the buoy by clouds, lack of sunglint correction, radiometric inaccuracy of the MOBY buoy (<5 % (Clark, et al., 2003)), the difference in measured wavelength between MOBY and Sentinel-2B and known gain coefficients (Clerc, 2018) not being applied to the Sentinel-2 data.

Given that the SNRs over this clear water surface fall far below the requirements for the ocean colour applications (Hu, et al., 2012), this is likely to the primary source of error in this validation exercise for the atmospheric correction of these Sentinel-2B tiles over the MOBY buoy.

Tamar Estuary: Spectral Signature

Figure 8 shows the spectra collected at various stations on the Tamar, these were chosen to show the range of spectra results observed in this study. There are two clear different spectral shapes for the data observed in Figure 8. The signature at station 4 and station 7 do not display a significant signature at ~650 nm and station 4 has a clear signature at ~500 nm. Stations 11, 16, 17 and 18 show a clear signature at ~560, ~650 and at ~ 810 nm.

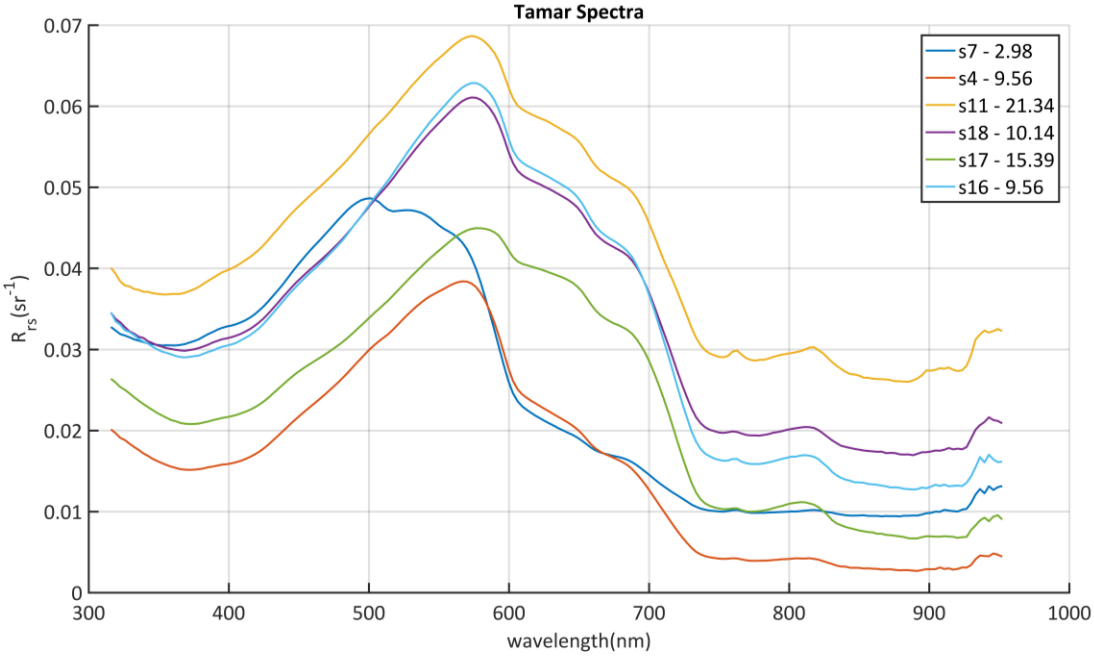

Figure 8: Spectral signature at six stations with varying SPM concentrations.

These results are similar to the results of Doxaran, et al. (2005) who observed spectral features at ~560, ~650 and ~800 nm in waters of the Tamar with an SPM concentration of 45 mg L^{-1}. In a region of the Tamar with lower total SPM (7 mg L^{-1}) they observed similar spectra to the spectra observed in this study at stations 4 and 7. The signature at ~560 nm is indicative of low absorption by chlorophyll, and the depression at ~440 nm is indicative of high absorption by chlorophyll pigments (Kirk, 2011).

Tamar Estuary: Modelled Sentinel-2A Spectra

Figure 9 shows the *in situ* spectra from the cruise on the 27th of March 2017 (top) and the spectra modelled in the bands of Sentinel-2A (middle). It also shows the spectra from the Senitnel-2A flyover on the 26th of March 2017 (bottom). Atmospheric correction was performed using the 865nm/2202nm (NIR/SWIR) band combination.

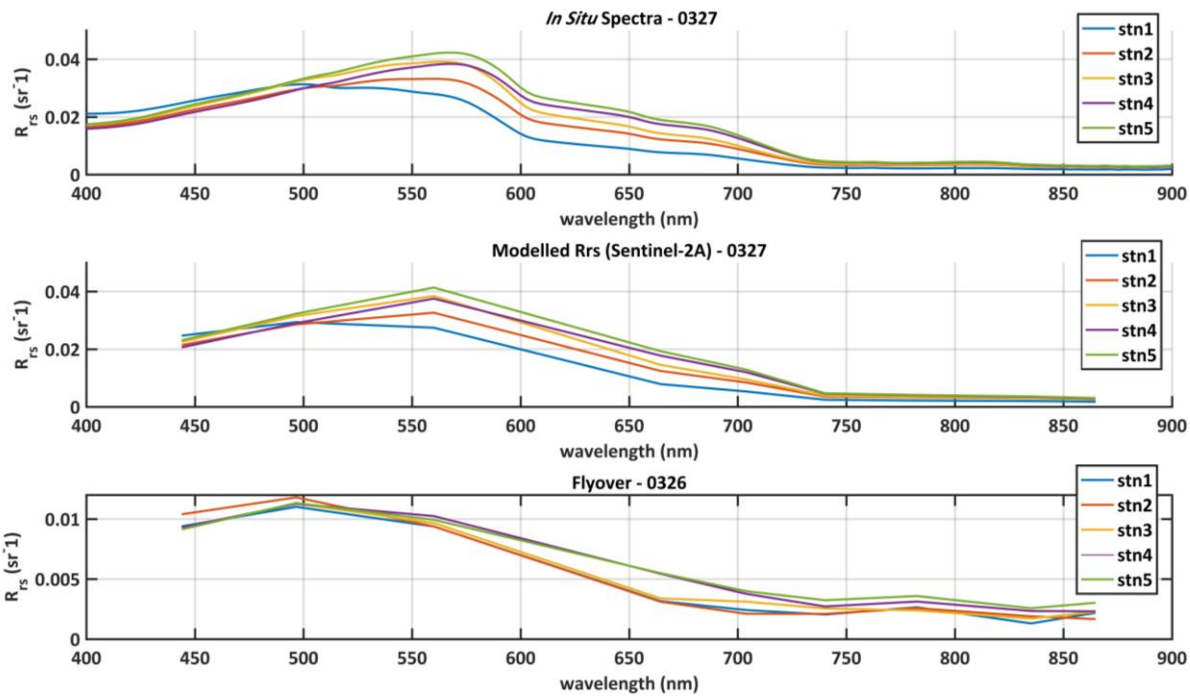

Figure 9: In situ, Sentinel-2A modelled and flyover spectra. Top: In situ spectra collected at five stations (in the lower Tamar/Sound) on the 27th of March 2017. Middle: In situ spectra modelled for the bands of Sentinel-2A. Bottom: BOA Rrs(λ) derived from the Sentinel-2A flyover (26th of March 2017) for the same five stations.

The modelled spectra (middle) fits the *in situ* spectra (top) reasonably well, but misses the sharp decline in $R_{rs}(\lambda)$ between 575 nm and 610 nm. This is due to the ‘jump’ in the Sentinel-2 bands between 560nm and 665nm (Table 1).

Figure 9 shows clear discrepancies in the $R_{rs}(\lambda)$ acquired *in situ* and the $R_{rs}(\lambda)$ derived from the atmospheric correction of the Senitnel-2A flyover. For example, at 550nm the *in situ* spectra reflectance values are between ~0.03 sr^{-1} and ~0.04 sr^{-1} whereas the Sentinel-2A derived R_{rs}(550nm) gives a reflectance value of ~0.01 sr^{-1}. These differences are observed from 400nm to 700nm, after which the spectra are of the same order (for station 1 *in situ* R_{rs}(782.2nm) = 0.0039 sr^{-1}, for station 1 flyover R_{rs}(782.5nm) = 0.0035 sr^{-1}). It is possible the differences in spectra could be due to tidal or meteorological variations. To clarify whether or not these factors were influential, the tidal and rainfall data will be discussed.

In situ spectra were collected between 10:00 UTC and 12:00 UTC; the Sentinel-2A flyover was at 11:20 UTC (the day prior). The tidal state during the *in situ* survey was between LW – 1.5 (at 10:00 UTC) and LW + 0.5 (at 12:00 UTC), at the time of the flyover the tidal state was at LW + 0.5 (the day before). Total rainfall for the 25th, 26th and 27th of March 2017 was 1.2, 0.2 and 0.2 mm respectively. Given the similarity in tidal state and the fact there were no significant rainfall events occurring around the dates of flyover or *in situ* measurements, it is assumed that the five stations (Figure 9) would have similar optical properties at the time the measurements were taken. Thus, it is assumed that the discrepancies observed in Figure 9 occur due to inaccuracies in atmospheric correction, this is supported by Figure 7 and the discussion thereafter. As discussed in the previous section, inadequate SNRs in the bands used for atmospheric correction can lead to noise and systematic error across the visible spectrum (Hu, et al., 2012), this is the most likely explanation for the inaccurate atmospheric correction. Potential SNR performance issues are supported by the fact this is a land satellite, and thus the spectral resolution is coarse in comparison to traditional ocean colour satellites (European Space Agency, 2015). This is also supported by the clear water SNR results of Pahlevan, et al, (2017) (Table 1), however are not directly relevant as the Tamar estuary is a coastal region with turbid waters (Dyer, 1995). For turbid coastal waters the reflected signal in the blue bands is often lower than for clear waters. This is commonly due to the absorption of light by Chlorophyll-a and coloured dissolved organic matter (CDOM) (Hu, et al., 2012). This may explain the large differences in $R_{rs}(\lambda)$ at the blue end of spectrum (for station 1 *in situ* R_{rs}(497.6nm) = 0.033 sr^{-1}, for station 1 flyover R_{rs}(496.6) = 0.011 sr^{-1}; for station 1 *in situ* R_{rs}(444.8nm) = 0.02 sr^{-1}, for station 1 flyover R_{rs}(443.9) = 0.009 sr^{-1}), as a depressed signal in the blue bands may lead to lower SNRs.

Tamar Estuary: Empirical SPM Algorithm

Figure 10 shows the results of the four surface reflectance ratios as a function of SPM concentration. Additional green/blue band ratios were derived as the fit for the NIR and red ratios were poor. Based on the statistics (Table 5), the best performing retrieval algorithm was observed using the $R_{rs}(560\text{nm})/R_{rs}(443\text{nm})$ ratio (top left in Figure 10, R^2 = 0.761, p-value = 0.000997 ($\alpha = 0.05$)).

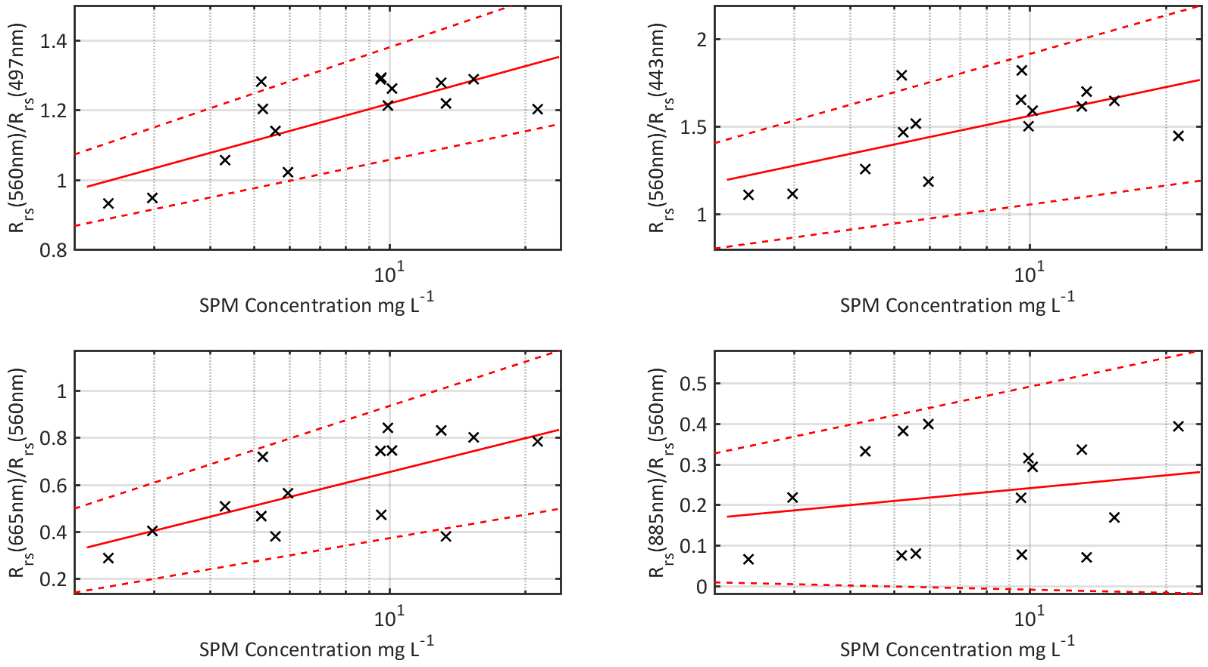

Figure 10: Log linear regressions for four band ratios as a function of SPM with confidence intervals. SPM concentration represents the total SPM measured at each station, comprising both inorganic and organic materials. Band ratios used are as follows: top left (560nm/497nm), top right (560nm/443nm), bottom left (665nm/560nm) and bottom right (885nm/560nm).

Table 5: Equation, p-value and R^2 for the four log linear regressions (Figure 10).

$R_{rs}(\lambda)/R_{rs}(\lambda)$ (nm)	Equation	R^2	p-value
560nm/497nm	$y = 0.1546\ln(x) + 0.8627$	0.761	0.000997
560nm/443nm	$y = 0.2367\ln(x) + 1.016$	0.633	0.0113
665nm/560nm	$y = 0.2073\ln(x) + 0.1763$	0.670	0.0063
885nm/560nm	$y = 0.0456\ln(x) + 0.136$	0.212	0.436

It is likely that the red and NIR based algorithms performed poorly (R^2 = 0.67 and R^2 = 0.212) due to the small spectral signal at this end of the spectrum (650 - 900nm) observed in these waters (Figure 9). This is because any errors in data collection would have profound effects of the results, as the spectral signal is so small. In the Gironde estuary, Doxaran, et al. (2003) observed refelctance values in the ~800nm region as high as the reflectance in the ~600 nm region. They also observed that with increasing SPM concentrations the spectral signitaure at ~800nm increased rapidly from 39 mg L^{-1} to 527 mg L^{-1}, but the signature at ~600nm remained relatively constant.

Tamar Estuary: SPM Maps (26th March 2017/25th January 2017)

Given that the $R_{rs}(560\text{nm})/R_{rs}(443\text{nm})$ ratio performed best (Table 5), this relationship was applied to the Sentinel-2A tile from the 26th of March 2017 and the 25th of January. This was achieved using the following algorithm:

$$SPM\ (mg\ L^{-1}) = e^{\frac{\frac{R_{rs}(560)}{R_{rs}(497)} - 0.8627}{0.1546}}$$

Equation 5: Empirically Derived SPM Algorithm

Figure 11 shows Equation 5 applied to the Senitnel-2A tile from the 26th of March 2017. Figure 12 shows Equation 5 applied to the Senitnel-2A tile from the 25th of January 2017. Given the tidal state (LW + 0.5) when the image was taken (Figure 11) it is expected that the ETM would be in the lower reaches of the estuary (Dyer, 1995). Neap tide was approximately 1 week prior to the flyover, thus the ETM would be expected to hold more than during the standard neap (max 200 mg L^{-1}) but less than during the spring tide (max 2 – 3 g L^{-1}) (Dyer, 1995).

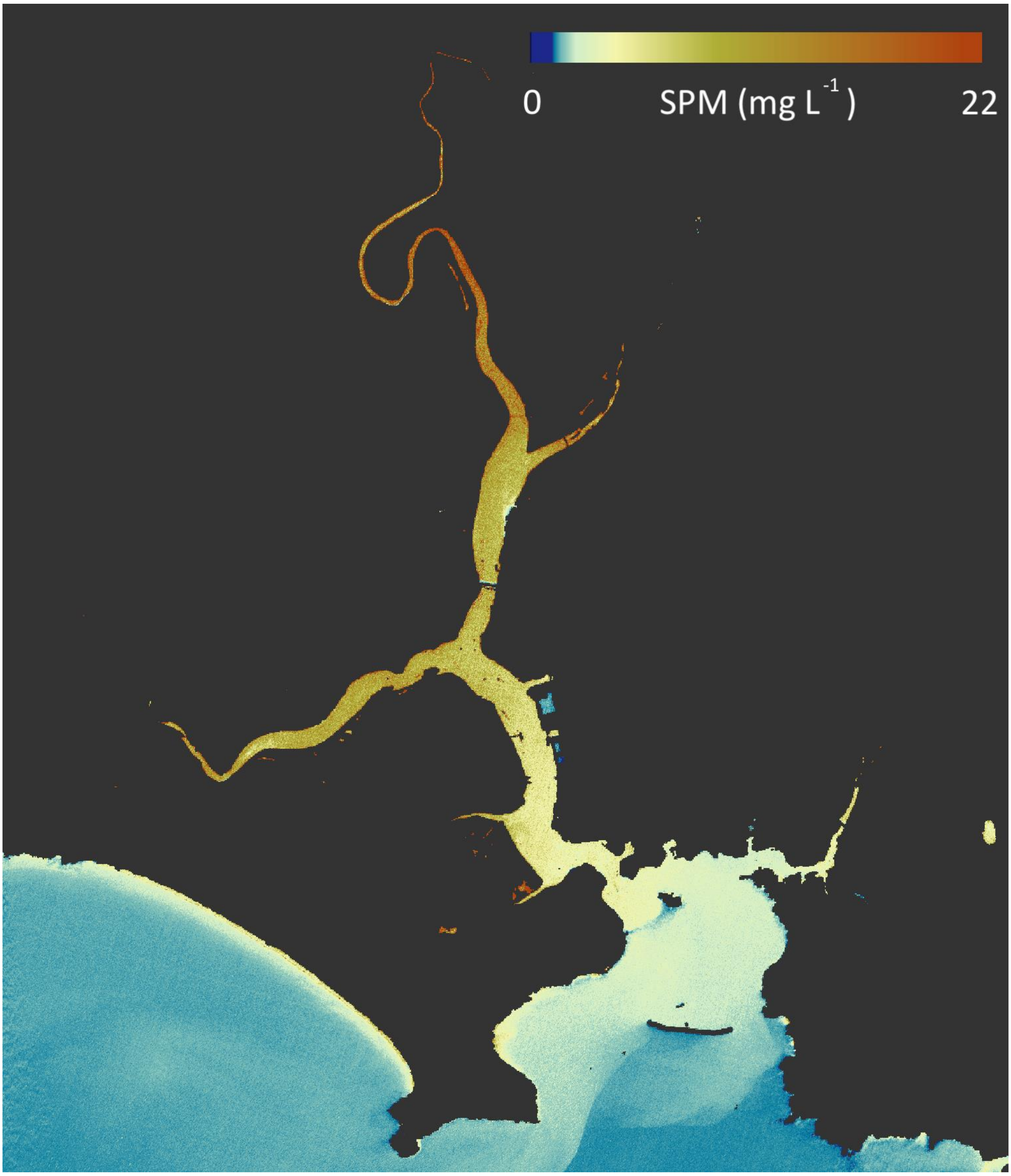

Figure 11: SPM algorithm applied to a Sentinel-2A tile over the Tamar estuary (26th of March 2017). Atmospheric correction was performed using the 865nm/2202nm band ratio. Credit: ESA/Sentinel-2A/MSI – *CC BY-SA IGO 3.0*. This tile was adapted under the Applicable License, as set forth in Article 4b of the *CC BY-SA 3.0 IGO* licence.

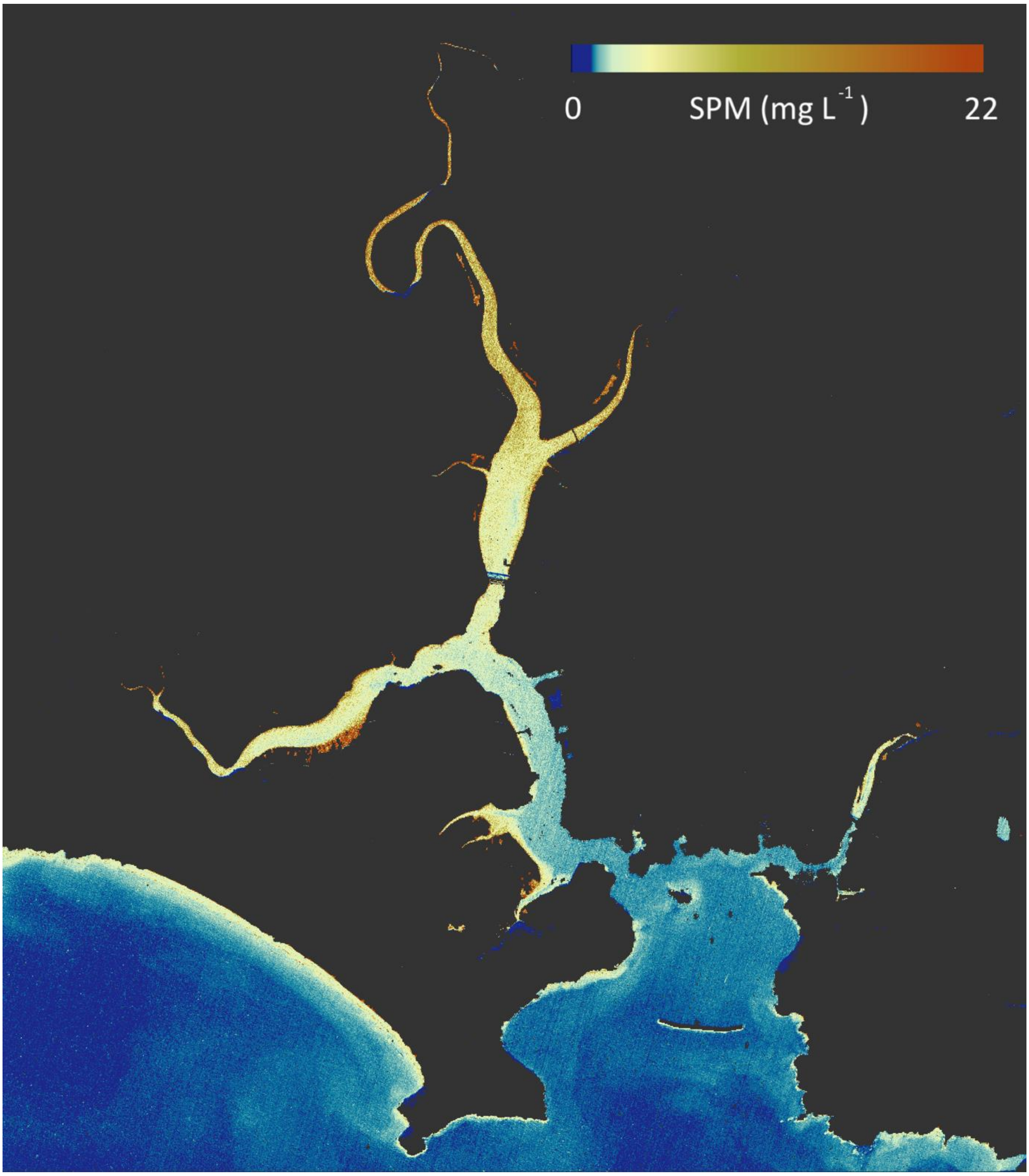

Figure 12: SPM algorithm applied to a Sentinel-2A tile over the Tamar estuary (25th of January 2017). Atmospheric correction was performed using the 865nm/2202nm band ratio. Credit: ESA/*Sentinel-2A*/*MSI* – CC BY-SA IGO 3.0*.* This tile was adapted under the Applicable License, as set forth in Article 4b of the CC BY-SA 3.0 IGO licence.

During this flyover (Figure 12) the tidal state was LW + 1.5. Thus, it is expected that SPM concentrations would be lower closer to the Sound due to the influence of sea water (compared to Figure 11). This appears to be true as concentrations are in the blue colour region (0 – 2 mg L^{-1}) further up the estuary than in Figure 11. During winter months, river flow rate generally increases in comparison to spring and summer due to increased precipitation rates (Dyer, 1995). Given this factor one would expect the concentration of SPM in the estuary to increase. This is not apparent when comparing Figure 12 (winter) to Figure 11 (spring). This may be explained by the fact that in the 10 days prior to the January flyover less than 1 mm of rain fell. It is also important to consider seasonal differences in terms of constituents in the water column and in the atmosphere as both will affect the results of the algorithm. For example it is likely that due to shifts in the light regime more plankton would be present in the water column in March (Figure 11) than in January (Figure 12). This would lead to significant differences in light absorption and scattering especially in the green and blue wavelengths the algorithm was applied to.

The SPM values in both images suggest the algorithm has underestimated the total SPM in the estuary. This can be attributed to a number of factors. Firstly, the inaccuracies in atmospheric correction described in the first section of this report which arise primarily due to inadequate SNRs (Pahlevan, et al., 2017). Further issues arise from inaccurate aerosol models, the lack of application of know gain coefficients (Clerc, 2018), adjacency (Otterman & Fraser, 1979) and sunglint effects. All of these factors increase the probability that the weak water-leaving radiance signal over the waters of the Tamar will be inaccurately derived, leading to inaccuracies in the final algorithm. The results of Doxaran, et al. (2005) showed that in the Tamar the blue to green signal (400 – 600 nm) is severly depressed in regions of the Tamar with higher SPM values. These results therefore demonstrate that total SPM is not a function of these wavelengths and thus the algorithm developed in this project will not work in more turbid waters. This is supported by Tassan (1993) who demonstrated that chlorophyll and total SPM do not co-vary in estuarine and coastal waters due to the presence of particulate matter from runoff, resuspension effects and shore erosion.

The limitations of developing an effective algorithm for the quantification of SPM in the Tamar estuary in this study were due to inaccurate amtospheric correction mainly caused by inadequate SNRs and an insufficient range of SPM values and accompanying spectral data.

Conclusion

In the first section of this project the radiometric performance of Sentinel-2B was quantified using *in situ* above-surface reflectance acquired by the MOBY buoy, in case 1 waters. The radiometric performance was tested using three atmospheric band combinations. The results showed that each method broke down in the green and red spectral regions (RD -27 – -87 % at 560nm, RD 312 – 440 % at 665nm) compared to the blue spectral region (443nm (RD 4 – 11 %) and 491nm bands (RD -8 – -17 %)). The primary reason for this was due to inadequate SNRs, caused by the high spatial resolution and wide bandwidths of the MSI sensor. In the second section of this project *in situ* SPM and spectral data collected in the Tamar was used to derive four empirical algorithms each using a different Sentinel-2A band ratio. The best fitting relationship was derived from the $R_{rs}(560\text{nm})/R_{rs}(443\text{nm})$ band ratio ($R^2 = 0.761$, p-value = 0.000997 ($\alpha = 0.05$)). After the algorithm was derived it was applied to a Sentinel-2A image from the 26th of March 2017 and the 25th of January 2017. With comparisons from the literature the SPM map underestimated SPM considerably in each image. This was a result of using the green blue ratio which does not represent higher SPM in the upper reaches of the estuary. To derive an effective SPM algorithm for the Tamar estuary, more SPM samples in conjunction with spectral surveys must be carried out. In addition to this, considerable improvements need to be implemented into the atmospheric correction methodology.

If achievable, Sentinel-2 would serve as an effective tool for quantifying SPM in the Tamar estuary.

Acknowledgements

I'd like to thank my supervisor Dr Jill Schwarz for guidance on this project. I'd also like to thank the students of the MAR518 module and again the module leader (Dr Jill Schwarz) for the data collected in the Tamar.

References

Acker, J. et al., 2002. Satellite remote sensing observations and aerial photography of storm-induced neritic carbonate transport from shallow carbonate platforms. *International Journal of Remote Sensing,* 23(14), pp. 2853-2868.

Alldredge, A. & Silver, M., 1988. Characteristics, dynamics and significance of marine snow. *Progress in oceanography,* 20(1), pp. 41-82.

Allen, G. P. et al., 1980. Effects of tides on mixing and suspended sediment transport in macrotidal estuaries. *Sediment Geology,* Volume 26, pp. 69-90.

Babin, M. & Stramski, D., 2002. Light absorption by aquatic particles in the near-infrared spectral region. *Limnology and Oceanography,* Volume 47, pp. 911-915.

Banse, K., Falls, C. & Hobson, L., 1963. A gravimetric method for determining suspended matter in sea water using Millipore filters. *Deep Sea Research and Oceanographic Abstracts,* 10(5), pp. 639-642.

Bingham, F. & Lukas, R., 1996. Seasonal cycles of temperature, salinity and dissolved oxygen observed in the Hawaii Ocean Time-series. *Deep Sea Research Part II: Topical Studies in Oceanography,* 43(2-3), pp. 199-213.

Bodhaine, B., Wood, N., Dutton, E. & Slusser, J., 1999. On Rayleigh optical depth calculations. *Journal of Atmospheric and Oceanic Technology,* 16(11), pp. 1854-1861.

Bowers, D. & Binding, C., 2006. The optical properties of mineal suspended particles: A review and synthesis. *Estuarine, Coastal and Shelf Science,* Volume 67, pp. 219-300.

Bowers, D., Boudjelas, S. & Harker, G., 1998. The distribution of fine suspended sediments in the surface waters of the Irish Sea and its relation to tidal stirring. *International Journal of Remote Sensing,* 19(14), pp. 2789-2805.

Clark, D. et al., 2000. MOBY, a radiometric buoy for performance monitoring and vicarious calibration of satellite ocean color sensors: measurement and data analysis protocols. *Ocean Optics Protocols for Satellite Ocean Color Sensor Validation, Revision, 4,* pp. 3-34.

Clark, D. et al., 2003. MOBY, a radiometric buoy for performance monitoring and vicarious calibration of satellite ocean color sensors: measurement and data analysis protocols. *Ocean Optics Protocols for Satellite Ocean Color Sensor Validation, Revision, 4,* pp. 3-34.

Clerc, S., 2018. *S2 MPC Data Quality Report,* Paris: ESA.

D'Odorico, P., Gonsamo, A., Damm, A. & Schaepman, M., 2013. Experimental evaluation of Sentinel-2 spectral response functions for NDVI time-series continuity. *IEEE Transactions on Geoscience and Remote Sensing,* 51(3), pp. 1336-1348.

Donlon, C. et al., 2012. The global monitoring for environment and security (GMES) sentinel-3 mission. *Remote Sensing of Environment,* Volume 120, pp. 37-57.

Doxaran, D., Castaing, P. & Lavender, S., 2006. Monitoring the maximum turbidity zone and detecting fine-scale turbidity features in the Gironde estuary using high spatial resolution satellite sensor. *International Journal of Remote Sensing,* 27(11), pp. 2303-2321.

Doxaran, D., Cherukuru, R. & Lavender, S., 2005. Use of reflectance band ratios to estimate suspended and dissolved matter concentrations in estuarine waters. *International Journal of Remote Sensing,* 26(8), pp. 1763-1769.

Doxaran, D., Froidefond, J. & Castaing, P., 2003. Remote-sensing reflectance of turbid sediment-dominated waters. Reduction of sediment type variations and changing illumination conditions effects by use of reflectance ratios. *Applied Optics,* 42(15), pp. 2623-2634.

Doxaran, D., Froidefond, J., Castaing, P. & Babin, M., 2009. Dynamics of the turbidity maximum zone in a macrotidal estuary (the Gironde, France): Observations from field and MODIS satellite data. *Estuarine, Coastal and Shelf Science,* 81(3), pp. 321-332.

Doxaran, D. & Lavender, S. J., n.d. Location of the Maximum Turbidity Zone and detection of fine- scale turbidity features in estuaries using high spatial resolution satellite (SPOT, Landsat) and airborne (CASI) data.

Drusch, M. et al., 2012. Sentinel-2: ESA's Optical High-Resolution Mission for GMES Operational Services. *Remote Sensing of Environment,* Volume 120, pp. 25-36.

Dyer, K., 1995. Sediment Transport Processes In Estuaries. In: G. Perillo, ed. *Developments in Sedimentology.* s.l.:Elsevier Science B. V., pp. 423-449.

Etcheber, H. et al., 2011. Monitoring water quality in estuarine environments: lessons from the MAGEST monitoring program in the Gironde fluvial-estuarine system. *Hydrology and Earth System Sciences,* 15(3), pp. 831-840.

European Space Agency, 2015. *Sentinel-2 User Handbook,* Paris: ESA.

European Union, 2008. Directive 2008/56/EC of the European Parliament and of the Council of 17 June 2008 establishing a framework for community action in the field of marine environmental policy (Marine Strategy Framework Directive). *Offical Journal of the European Union,* Volume 164, pp. 19-40.

Fettweis, M. & Van den Eynde, D., 2003. The mud deposits and the high turbidity in the Belgian–Dutch coastal zone, Southern bight of the North Sea. *Continental Shelf Research,* Volume 23, pp. 669-691.

Forget, P. & Ouillon, S., 1998. Surface suspended matter off the Rhone river mouth from visible satellite imagery. *Oceanologica Acta,* Volume 21, pp. 739-749.

Franz, B., Bailey, S., Kuring, N. & Werdell, P., 2015. Ocean color measurements with the Operational Land Imager on Landsat-8: implementation and evaluation in SeaDAS. *Journal of Applied Remote Sensing,* 9(1), p. 096070.

Gao, B., Montes, M., Davis, C. & Goetz, A., 2009. Atmospheric correction algorithms for hyperspectral remote sensing data of land and ocean. *Remote Sensing of Environment,* Volume 113, pp. S17-S24.

Gatti, A. & Bertolini, A., 2017. *Sentinel-2 products specification document.* [Online] Available at: https://sentinel.esa.int/documents/247904/349490/S2_MSI_Product_Specification.pdf [Accessed 28 January 2018].

Gatti, A. & Galoppo, A., 2018. Sentinel-2 Products Specification Document, s.l.: esa.

Gernez, P. et al., 2015. Toward Sentinel-2 high resolution remote sensing of suspended particulate matter in very turbid waters: SPOT4 (Take5) Experiment in the Loire and Gironde Estuaries. *Remote Sensing,* 7(8), pp. 9507-9528.

Google Maps, 2018. *Google Maps.* Available at: https://www.google.co.uk/maps/@20.7529386,-156.9681477,9.25z [Accessed 18 April 2018].

Gordon, H., Du, T. & Zhang, T., 1997. Remote sensing of ocean color and aerosol properties: resolving the issue of aerosol absorption. *Applied Optics,* 36(33), pp. 8670-8684.

Gordon, H. R. & Wang, M., 1994. Retrieval of water-leaving radiance and aerosol optical thickness over the oceans with SeaWiFS: a preliminary algorithm. *Applied Optics,* 33(3), pp. 443-452.

Grabemann, I., Uncles, R. J., Krause, G. & Stephens, J. A., 1997. Behaviour of turbidity maxima in the Tamar (UK) and Weser (FRG) estuaries. *Estuarine, Coastal and Shelf Science,* 45(2), pp. 235-246.

Harker, G., 1997. A comparison between optical measurements made in the field in the laboratory, and the development of an optical model. *Phd Thesis, Univeristy of Wales, Bangor, U.K.*

Harmel, T. et al., 2018. Sunglint correction of the Multi-Spectral Instrument (MSI)-SENTINEL-2 imagery over inland and sea waters from SWIR bands. *Remote Sensing of Environment,* Volume 204, pp. 308-321.

Hayward, T., 1991. Primary production in the North Pacific Central Gyre: a controversy with important implications. *Trends in ecology and evolution,* 6(9), pp. 281-284.

Hoppe, H., 1984. Attachment of bacteria: advantage or disadvantage for survival in the aquatic environment. In: *Microbial adhesion and aggregation, Life Sciences Research Report, 31.* New York: Springer-Verlag, pp. 283-301.

Hu, C. et al., 2012. Dynamic range and sensitivity requirements of satellite ocean color sensors: learning from the past. *Applied Optics,* 51(25), pp. 6045-6062.

IOCCG, 2000. Remote Sensing of Ocean Colour in Coastal, and Other Optically-Complex, Waters. In: S. Sathyendranath, ed. *Reports of the International Ocean-Colour Coordinating Group.* Dartmouth: IOCCG.

Jackson, G. et al., 1997. Particle size spectra between 1 µm and 1 cm at Monterey Bay determined using multiple instruments. *Deep Sea Research Part I: Oceanographic Research Papers,* 44(11), pp. 1739-1767.

Jones, S. et al., 1998. Aggregation and resuspension of suspended particulate matter at a seasonally stratified site in the southern North Sea: physical and biological controls. *Continental Shelf Research,* 18(11), pp. 1283-1309.

Karl, D. & Lukas, R., 1996. The Hawaii Ocean Time-series (HOT) program: Background, rationale and field implementation. *Deep Sea Research Part II: Topical Studies in Oceanography,* 43(2-3), pp. 129-156.

Kirk, J. T. O., 2011. Absorption of light within the aquatic medium. In: *Light and Photosynthesis in Aquatic Ecosystems, Third Edition.* New York: Cambridge university press, pp. 50-95.

Lacroix, G. et al., 2007. Validation of the 3D biogeochemical model MIRO&CO with field nutrient and phytoplankton data and MERIS-derived surface chlorophyll a images. *Journal of Marine Systems,* Volume 64, pp. 66-88.

Lantzanakis, G., Mitraka, Z. & Chrysoulakis, N., 2017. Comparison of physically and image based atmospheric correction methods for Sentinel-2 satellite imagery. In: *Perspectives on Atmospheric Sciences.* Cham: Springer, pp. 255-261.

Lee, Z. et al., 2016. On the modeling of hyperspectral remote-sensing reflectance of high-sediment-load waters in the visible to shortwave-infrared domain. *Applied optics,* 55(7), pp. 1738-1750.

Liu, H. et al., 2017. Application of sentinel 2 MSI images to retrieve suspended particulate matter concentrations in Poyang Lake. *Remote Sensing,* 9(7), p. 761.

Matthews, M., 2011. A current review of empirical procedures of remote sensing in inland and near-coastal transitional waters. *International Journal of Remote Sensing,* 32(21), p. 6855–6899.

Maul, G., 2012. Introduction to satellite oceanography. In: s.l.:Springer Science and Business Media.

McCave, I., 1975. Vertical Flux of Particles in the Ocean. *Deep Sea Research,* Volume 22, pp. 491-502.

Mertes, L., Smith, M. & Adams, J., 1993. Estimating suspended sediment concentrations in surface waters of the Amazon River wetlands from Landsat images. *Remote Sensing of the Environment,* Volume 43, pp. 281-301.

Mobley, C. D., 1994. Light and Water: Radiative Transfer in Natural Waters. San Diego: CA: Academic.

Mobley, C. D., 1999. Estimation of the remote-sensing reflectance from above-surface measurements. *Applied Optics,* 38(36), pp. 7442-7455.

Morel, A. & Antoine, D., 1994. Heating rate within the upper ocean in relation to its bio-optical state. *Journal of Physical Oceanography,* 24(7), pp. 1652-1665.

Morel, A. & Prieur, L., 1977. Analysis of Variations in Ocean Color. *Limology and Oceanography,* 22(4), pp. 709-722.

Nechad, B., De Cauwer, V., Park, Y. & Ruddick, K., 2003. Suspended Particulate Matter (SPM) mapping from MERIS imagery. Calibration of a regional algorithm for the Belgian coastal waters. Frascati, Italy, ESA.

Nechad, B., Dogliotti, A., Ruddick, K. & Doxaran, D., 2016. Particulate Backscattering Retrieval from Remotely-Sensed Turbidity in Various Coastal and Riverine Turbid Waters. Prague, ESA.

Nechad, B., Ruddick, K. & Park, Y., 2010. Calibration and validation of a generic multisensor algorithm for mapping of total suspended matter in turbid waters. *Remote Sensing of Environment journal,* Volume 114, pp. 854-866.

Novo, E. M. M., Hansom, J. D. & Curran, P. J., 1989. The effect of sediment type on the relationship between reflectance and suspended sediment concentration. *International Journal of Remote Sensing,* 10(7), pp. 1283-1289.

Otterman, J. & Fraser, R., 1979. Adjacency effects on imaging by surface reflection and atmospheric scattering: cross radiance to zenith. *Applied Optics,* 18(16), pp. 2852-2860.

Pahlevan, N. et al., 2017. Sentinel-2 MultiSpectral Instrument (MSI) data processing for aquatic science applications: Demonstrations and validations. *Remote Sensing of Environment,* Volume 201, pp. 47-56.

Passow, U., Alldredge, A. & Logan, B., 1994. The role of particulate carbohydrate exudates in the flocculation of diatom blooms. *Deep Sea Research Part I: Oceanographic Research Papers,* 41(2), pp. 335-357.

Platt, T., Sathyendranath, S., Caverhill, C. & Lewis, M., 1988. Ocean primary production and available light: further algorithms for remote sensing. *Deep Sea Research Part A. Oceanographic Research Papers,* 35(6), pp. 855-879.

Shimwell, S., 1999. An investigation into the optical properties of North Sea coastal waters in relation to ocean colour remote sensing. *Doctoral dissertation, University of Southampton.*

Strickland, J. D. H. & Parsons, T. R., 1972. *A Practical Handbook of Seawater Analysis,* Ottawa: Fisheries Research Board of Canada Series.

Tassan, S., 1993. An improved in-water algorithm for the determination of chlorophyll and suspended sediment concentration from Thematic Mapper data in coastal waters. *International Journal of Remote Sensing,* 14(6), pp. 1221-1229.

Toming, K. et al., 2016. First Experiences in Mapping Lake Water Quality Parameters with Sentinel-2 MSI Imagery. *Remote Sensing,* 8(8), p. 640.

Uncles, R., Barton, M. & Stephens, J., 1994. Seasonal variability of fine-sediment concentrations in the turbidity maximum region of the Tamar Estuary. *Estuarine, Coastal and Shelf Science,* 38(1), pp. 19-39.

Uncles, R. J. & Stephens, J. A., 1989. Distributions of suspended sediment at high water in a macrotidal estuary. *Journal of Geophysical Research,* Volume 94, pp. 14395-14405.

Uncles, R. & Stephens, J., 1993. Nature of the turbidity maximum in the Tamar Estuary, UK. *Estuarine, Coastal and Shelf Science,* 36(5), pp. 413-431.

Van Raaphorst, W. et al., 1998. Distribution of suspended particulate matter in the North Sea as inferred from NOAA/AVHRR reflectance images and in situ observations. *Journal of Sea Research,* 38(3-4), pp. 197-215.

Vanhellemont, Q., 2017. *Overview of ACOLITE settings (20170718.0),* Brussels: Royal Belgian Institute of Natural Sciences.

Vanhellemont, Q. and Ruddick, K., 2016, May. Acolite for Sentinel-2: Aquatic applications of MSI imagery. In *Proc. the 2016 ESA Living Planet Symposium, ESA Special Publication SP-740*.

Vermote, E. et al., 2006. Second simulation of a satellite signal in the solar spectrum-vector (6SV). *6S User Guide Version, 3,* pp. 1-55.

Watanabe, F. et al., 2017. Remote sensing of the chlorophyll-a based on OLI/Landsat-8 and MSI/Sentinel-2A (Barra Bonita reservoir, Brazil). *Annals of the Brazilian Academy of Sciences.*

Yang, H. & Gordon, H., 1997. Remote sensing of ocean color: assessment of water-leaving radiance. *Applied Optics,* Volume 36, pp. 7887-7897.

Yepez, S. et al., 2017. Retrieval of suspended sediment concentrations using Landsat-8 OLI satellite images in the Orinoco River (Venezuela). *Comptes Rendus Geoscience,* 350(1-2), pp. 20-30.